

A Resource-Efficient Training Framework for Remote Sensing Text–Image Retrieval

Weihang Zhang^{a,c}, Jihao Li^{a,b}, Shuoke Li^{a,b}, Ziqing Niu^{c,d}, Jialiang Chen^{a,b}, Wenkai Zhang^{a,c,*}, Xin Gao^{a,b} and Xian Sun^{a,b}

^aAerospace Information Research Institute, Chinese Academy of Sciences, Beijing, 100190, China

^bKey Laboratory of Network Information System Technology (NIST), Aerospace Information Research Institute, Chinese Academy of Sciences, Beijing, 100190, China

^cUniversity of Chinese Academy of Sciences, Beijing, 100190, China

^dSchool of Electronic, Electrical and Communication Engineering, University of Chinese Academy of Sciences, Beijing, 100190, China

ARTICLE INFO

Keywords:

Remote sensing text–image retrieval
Cross-modal retrieval
Resource efficiency
Transfer learning

ABSTRACT

Remote sensing text–image retrieval (RSTIR) aims to retrieve the matched remote sensing (RS) images from the database according to the descriptive text. Recently, the rapid development of large visual-language pre-training models provides new insights for RSTIR. Nevertheless, as the complexity of models grows in RSTIR, the previous studies suffer from suboptimal resource efficiency during transfer learning. To address this issue, we propose a computation and memory-efficient retrieval (CMER) framework for RSTIR. To reduce the training memory consumption, we propose the Focus-Adapter module, which adopts a side branch structure. Its focus layer suppresses the interference of background pixels for small targets. Simultaneously, to enhance data efficacy, we regard the RS scene category as the metadata and design a concise augmentation technique. The scene label augmentation leverages the prior knowledge from land cover categories and shrinks the search space. We propose the negative sample recycling strategy to make the negative sample pool decoupled from the mini-batch size. It improves the generalization performance without introducing additional encoders. We have conducted quantitative and qualitative experiments on public datasets and expanded the benchmark with some advanced approaches, which demonstrates the competitiveness of the proposed CMER. Compared with the recent advanced methods, the overall retrieval performance of CMER is 2%–5% higher on RSITMD. Moreover, our proposed method reduces memory consumption by 49% and has a 1.4x data throughput during training. The code of the CMER and the dataset will be released at [Link].

1. Introduction

Continuous advances in earth observation technology and the increasing number of satellites have accelerated the acquisition of high-resolution, multi-source remote sensing (RS) image data (Chi et al., 2016; Amani et al., 2020). How to effectively extract critical information of interest from massive RS images has become an important research direction in RS image processing (Zhou et al., 2023; Li et al., 2020).

RS image retrieval has been a hot research topic in the last decade (Sun et al., 2022, 2023; Blumenstiel et al., 2024). Many RS image retrieval methods have emerged, among which the cross-modal retrieval methods have gained growing interest from researchers due to their subjectivity. Concretely, the cross-modal retrieval methods contain multiple modalities in query, including multispectral images (Sun et al., 2024; Xiong et al., 2022), sketches (Fang et al., 2021), audio (Mao et al., 2018; Ning et al., 2021), ground panorama (Ren et al., 2023; Li et al., 2024a), and text (Liu et al., 2024a; Ma et al., 2024).

Remote sensing text–image retrieval (RSTIR) aims to retrieve RS images by corresponding descriptions (Zhang et al., 2023). According to the patterns of cross-modal interaction, RSTIR methods can be divided into two categories: dual-stream and single-stream methods. Text and images are encoded independently in the dual-stream methods (Zhang et al., 2023; Pan et al., 2023b). The single-stream methods perform cross-modal feature fusion during the early feature

*Corresponding author. This work was supported by the National Key R&D Program of China under grant 2022ZD0118402.

✉ zhangweihang21@mails.ucas.ac.cn (W. Zhang); lijihao17@mails.ucas.edu.cn (J. Li); lisk@aircas.ac.cn (S. Li); niuziqing21@mails.ucas.ac.cn (Z. Niu); chenjl@aircas.ac.cn (J. Chen); zhangwk@aircas.ac.cn (W. Zhang); gaixin@aircas.ac.cn (X. Gao); sunxian@aircas.ac.cn (X. Sun)

ORCID(s):

extraction stage. Recently, large pre-trained visual-language models have achieved significant success (Radford et al., 2021; Li et al., 2021, 2023), bringing new insights for RSTIR (Li et al., 2024b). The parameter-efficient transfer learning (PETL) methods strive to transfer the prior information in pre-trained tasks to downstream tasks through fine-tuning a small set of parameters in the large pre-trained models (Lialin et al., 2023), which has gained widespread popularity.

Although some progress has been made in RSTIR, one remaining challenge is improving the resource efficiency of transfer learning as the complexity of pre-trained models increases in RSTIR.

First, the current transfer learning methods for RSTIR suffer from suboptimal efficiency of GPU memory (Liu et al., 2024b; Yuan et al., 2023; Djoufack Basso, 2022). Even if few parameters are fine-tuned in previous superior methods (Liu et al., 2024b; Yuan et al., 2023), substantial intermediate activations still require computation and storage during training. In addition, the RS domain is more challenging during transfer learning. It is attributable to the high complexity of RS images, especially with multi-scale objects (Chen et al., 2023). Conventional methods often encounter interference from background noise when extracting visual features of targets with a small pixel proportion. The Focus-Adapter is proposed to tackle the above issue. The Focus-Adapter adopts the side branch architecture to improve the efficiency of memory utilization. Moreover, the focus layer is devised to emphasize the regionally salient feature of small targets. It can suppress the interference of background pixels for small target feature extraction.

To enhance data efficacy, we propose a plug-and-play augmentation technique that combines the specific content data with land cover categories. Recent mainstream RSTIR approaches neglect the substantial prior knowledge provided by the land cover categories (Pan et al., 2023b). We regard RS scene categories as metadata tags (Espinoza-Molina and Datcu, 2013) that serve as the prompt for the concrete query text. The scene label augmentation can shrink the retrieval space and mitigate mismatches between scenarios without increasing extra memory consumption. We also propose the negative sample recycling strategy to expand the negative sample pool. The sampling pool of negative samples in traditional methods is limited by the current mini-batch data, which is constrained by the available memory of hardware (Zhang et al., 2023; Yuan et al., 2023). We recycle the negative samples of previous iterations for the contrastive learning of current iteration data, which can better sample the underlying semantic space (He et al., 2020) of RS images.

Our contributions can be summarized as follows.

- We propose a computation and memory-efficient retrieval framework for RSTIR. To the best of our knowledge, CMER is the first framework dedicated to improving resource efficiency beyond parameter efficiency during training.
- We propose the Focus-Adapter, a side branch architecture with the focus layer as the core component. The Focus-Adapter improves the efficiency of GPU memory and emphasizes the regionally salient feature of small targets.
- To enhance the efficacy of training data, we innovatively regard RS scene categories as metadata tags and recycle the negative samples of previous iterations.
- We extend the benchmark with some excellent methods and conduct extensive experiments, which show that our novel CMER framework outperforms recent methods by a clear margin.

2. Related work

2.1. Remote sensing text-image retrieval

RSTIR aims to exploit the semantic information in textual data to retrieve the corresponding RS images. Currently, prevalent methods for RSTIR can be categorized into two types based on the patterns of cross-modal interaction: single-stream and dual-stream methods.

The dual-stream methods maintain independence in extracting image-text features without cross-modal feature fusion. Therefore, the dual-stream method can independently extract embedding vectors offline from different modalities. A multi-language framework for RSTIR was proposed by Al Rahhal et al. (2022), which can support multi-language queries. To address the semantic noise in RSTIR, Pan et al. (2023a) designed a prior instruction representation framework that consists of two progressive attention encoder structures and a cluster-wise loss. Zhang et al. (2023) proposed a concise and effective alignment strategy based on curriculum learning. Yuan et al. (2023) investigated the PETL method for RSTIR and extended the benchmark.

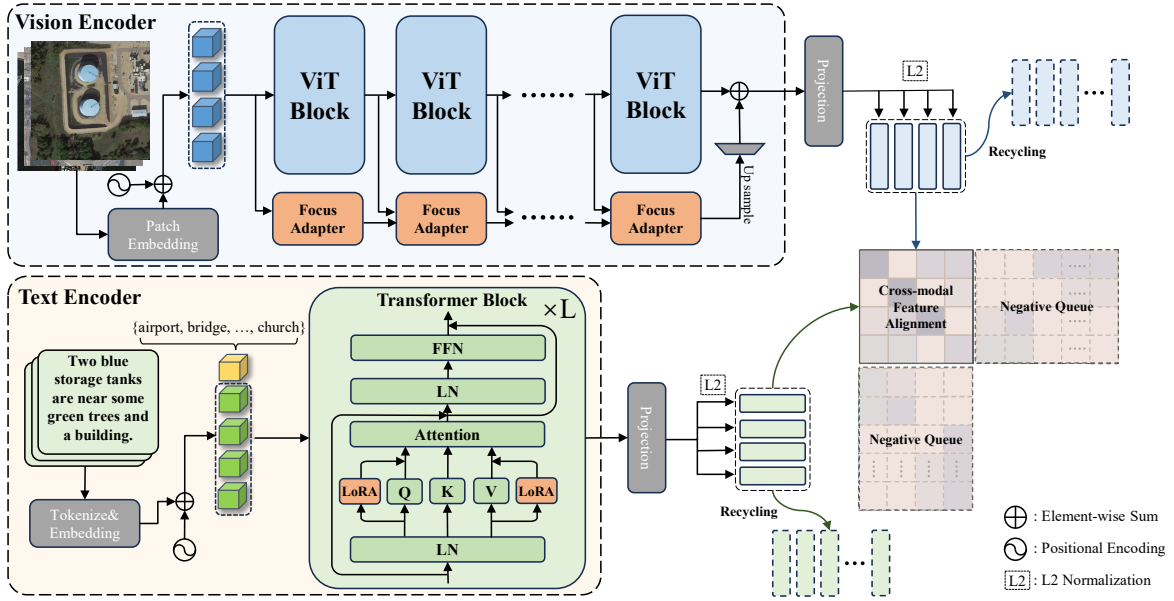


Figure 1: The pipeline of the proposed computation and memory-efficient retrieval (CMER) framework.

The single-stream methods perform cross-modal feature fusion during the early feature extraction stage. Yuan et al. (2022) designed a multi-source retrieval network that establishes the common space through multimodal shared coding. Tang et al. (2023) proposed the interacting-enhancing feature transformer for RSTIR. With increasing complexity, some recent RSTIR methods still have room for improvement in terms of efficiency and efficacy during training.

2.2. Transfer learning

The concept of transfer learning was first introduced by Pratt (1992). Many transfer learning methods have emerged in the last decade. Among them, PETL methods have received increasing attention (Lei et al., 2024).

The PETL methods train a fraction of the model parameters, which may be a new set of introduced parameters or a subset of the original model parameters. Houlsby et al. (2019) proposed the Adapter modules in order to improve the efficiency of fine-tuning large pre-trained models in natural language processing. Jiang et al. (2022) proposed the Cross-Modal Adapter for the multi-modal domain, which allows early interactions between multimodal. Zaken et al. (2021) introduced a sparse-finetuning method named BitFit. Hu et al. (2021) introduced the LoRA module for large language models, which reparameterizes the weight update matrix by the simple low-rank matrix. Similar to LoRA, Edalati et al. (2022) proposed the Kronecker Adapter. However, existing PETL algorithms are suboptimal in the more challenging RS domain because they are mainly tailored for downstream tasks, which are in the same domain as the pre-training tasks.

3. Method

3.1. Formulation

Figure 1 illustrates the pipeline of our framework. For RSTIR, features of the input image I and features of the description text T are obtained after cross-modal feature extraction. The obtained semantic embedding s_e and visual embedding v_e are normalized to the unit hypersphere for similarity measurement.

3.1.1. Visual representation

We utilize the Vision Transformer (ViT) (Dosovitskiy et al., 2020) as our primary visual encoder, initialized with pre-trained CLIP weights. To extract visual embedding vectors, the RS images are initially partitioned into $N \times N$ patches. The initial visual embedding sequence v^0 is obtained through sequence expansion and position encoding,

which can be expressed as:

$$\mathbf{v}^0 = [\mathbf{i}_{class}; \mathbf{W}_I \mathbf{i}_0; \dots; \mathbf{W}_I \mathbf{i}_{N^2-1}] + \mathbf{i}_{pos}, \quad (1)$$

where \mathbf{i}_{class} is the added CLS token, \mathbf{i}_l represents l -th image patch, and \mathbf{W}_I is the image embedding matrix. \mathbf{i}_{pos} is the position embedding vector. Subsequently, the initial visual embedding sequence \mathbf{v}^0 passes through D_v blocks of the ViT, which can be represented as:

$$\tilde{\mathbf{v}}^d = \text{MSA}(\text{LN}(\mathbf{v}^{d-1})) + \mathbf{v}^{d-1}, d \in [1, D_v], \quad (2)$$

$$\mathbf{v}^d = \text{FFN}(\text{LN}(\tilde{\mathbf{v}}^d)) + \tilde{\mathbf{v}}^d, d \in [1, D_v]. \quad (3)$$

where $\text{MSA}(\cdot)$ represents the Multi-head Self Attention module (Vaswani et al., 2017), $\text{LN}(\cdot)$ represents the layer normalization function and $\text{FFN}(\cdot)$ represents the Feed-Forward Network. $\tilde{\mathbf{v}}^d$ indicates the intermediate hidden features extracted by MSA module in d -th ViT block. \mathbf{v}^d is the final output of d -th block in ViT. The CLS token output by the D_v -th block is considered the image's global representation, and the visual embedding \mathbf{v}_e is obtained after normalization and projection.

3.1.2. Text representation

BERT (Devlin et al., 2018) is utilized to obtain semantic embedding \mathbf{s}_e , which is initialized with pre-trained CLIP weights. The description text is tokenized based on byte pair encoding, which is prefixed with the BOS token and suffixed with the EOS token. After token embedding and position encoding, the initial description text tokens can be represented as:

$$\mathbf{s}^0 = [\mathbf{M}_E \mathbf{t}_{bos}; \mathbf{M}_E \mathbf{t}_0; \dots; \mathbf{M}_E \mathbf{t}_L; \mathbf{M}_E \mathbf{t}_{eos}] + \mathbf{t}_{pos}, \quad (4)$$

where \mathbf{t}_{bos} refers to the token that represents the beginning of the sentence. \mathbf{t}_{eos} refers to the token that represents the ending of the sentence. \mathbf{t}_l stands for l -th token in the description text, and the preset maximum text processing length is denoted as L . \mathbf{M}_E refers to the token embedding matrix. \mathbf{t}_{pos} is the position embedding vector added to each token.

The initial tokens sequence \mathbf{s}^0 is fed to transformer blocks to obtain semantic embedding, which can be denoted as:

$$\tilde{\mathbf{s}}^d = \text{MSA}(\text{LN}(\mathbf{s}^{d-1})) + \mathbf{s}^{d-1}, d \in [1, D_s], \quad (5)$$

$$\mathbf{s}^d = \text{FFN}(\text{LN}(\tilde{\mathbf{s}}^d)) + \tilde{\mathbf{s}}^d, d \in [1, D_s]. \quad (6)$$

3.2. Focus-Adapter

Recent mainstream RSTIR methods based on transfer learning are sub-optimal regarding GPU memory efficiency during training (Yuan et al., 2023), (Djoufack Basso, 2022). Despite fine-tuning only a few parameters, a massive volume of intermediate activations still needs to be computed and stored during the training process.

For the sake of generality, we take a simple multi-layer perceptual network as an example and assume that layer i is the linear layer with $\mathbf{z}_n = \mathbf{z}_{n-1} \mathbf{W}_n + b_n$. According to the chain rule, the variables required computation in the backward propagation process include:

$$\frac{\partial L}{\partial \mathbf{W}_n} = \mathbf{z}_n^\top \frac{\partial L}{\partial \mathbf{z}_{n+1}}, \quad (7)$$

$$\frac{\partial L}{\partial b_n} = \frac{\partial L}{\partial \mathbf{z}_{n+1}}, \quad (8)$$

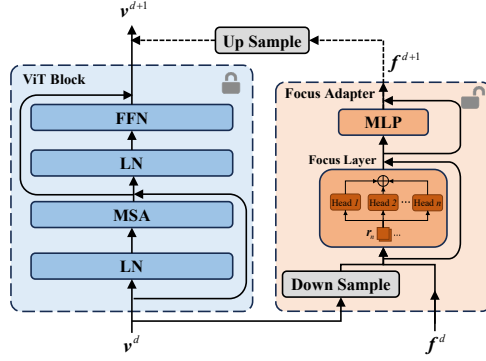


Figure 2: The implementation details of the proposed Focus-Adapter.

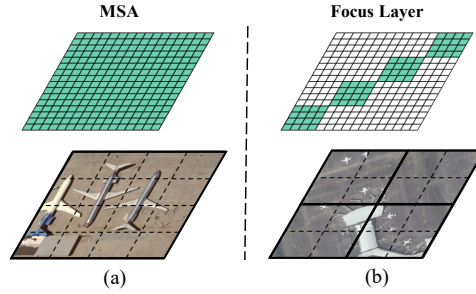


Figure 3: Region attention mechanism in the focus layer. The dotted lines in the RS images indicate the division of the image patches. The solid rectangles in the RS images represent the range of attention modeling. The above grid diagram shows the modeling relationships between image patches.

$$\frac{\partial L}{\partial \mathbf{z}_n} = \frac{\partial L}{\partial \mathbf{z}_{n+1}} \frac{\partial \mathbf{z}_{n+1}}{\partial \mathbf{z}_n} = \frac{\partial L}{\partial \mathbf{z}_{n+1}} \mathbf{W}_i^\top. \quad (9)$$

where L represents the overall loss function, \mathbf{W}_n and b_n denote the weight matrix and bias vector of the n -th layer, respectively. \mathbf{z}_n denotes the intermediate activation of the n th layer.

As demonstrated in Eq. (7) and Eq. (9), the memory footprint consists of two items: intermediate activation \mathbf{z}_n , and parameters \mathbf{W}_n that need to be updated. Previous RSTIR methods (Yuan et al., 2023) reduce the size of trainable parameters \mathbf{W}_n but neglect the computation and storage of activation \mathbf{z}_n .

To further enhance computation and memory efficiency, we propose the novel Focus-Adapter. As shown in Fig. 2, inspired by Zhang et al. (2020), deployment of the side branch decreases the computation and storage of activations when constructing the computational graph:

$$\mathbf{h}^d = \mathbf{v}^d \mathbf{W}_{down} + \mathbf{f}^d + b, d \in [1, D_f]. \quad (10)$$

where \mathbf{v}^d represents the feature of d -th block in the main branch calculated from Eq. (3), and \mathbf{f}^d represents the feature of d -th adapter in the side branch. \mathbf{W}_{down} serves as the shared downsample matrix, and b serves as the bias item.

Moreover, multi-scale variation is one of the main properties in RS images (Chen et al., 2023). For images with relatively large regions of interest, as shown in Fig. 3(a), it seems reasonable to utilize features of all patches to compute the attention score when extracting visual features. However, for images with smaller and more dispersed targets, as shown in Fig. 3(b), long-range modeling (Vaswani et al., 2017) may introduce background interference and computational redundancy.

Inspired by the local inductive bias of the CNN (He et al., 2016), the focus layer is designed to reduce the interference from the background by selectively emphasizing the regionally salient feature of small targets. Specifically,

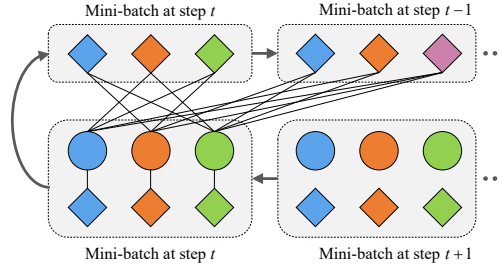


Figure 4: The queue update process in the negative sample recycling strategy. Diamonds represent visual features, and semantic features are represented by circles. The same color indicates the same category.

we introduce the local inductive bias of CNN (He et al., 2016). The feature \mathbf{h}^d calculated from Eq. (10) is first partitioned into distinct regions $[\mathbf{r}_1, \mathbf{r}_2, \dots, \mathbf{r}_N]$ according to the size of focus field. As shown in Fig. 3, the representation of regionally salient features is enhanced by the region attention mechanism, which is aimed at suppressing background pixel interference in long-range modeling. The above process can be represented as:

$$\text{head}_i = [\mathbf{r}_1, \mathbf{r}_2, \dots, \mathbf{r}_N] \mathbf{W}_i + b_i, i \in [0, H], \quad (11)$$

$$\tilde{\mathbf{f}}^d = [\text{head}_0, \text{head}_1, \dots, \text{head}_H] + \mathbf{h}^{d-1}, d \in [1, D_f], \quad (12)$$

$$\mathbf{f}^d = \tilde{\mathbf{f}}^d \mathbf{W}_d + \tilde{\mathbf{f}}^d, d \in [1, D_f]. \quad (13)$$

where head_i represents the salient feature emphasized by i -th attention head, and the enhanced region feature in d -th Focus-Adapter is denoted as $\tilde{\mathbf{f}}^d$. The total number of the Focus-Adapter is D_f .

3.3. Scene label augmentation

Recent mainstream RSTIR approaches primarily concentrate on specific content (Sudha and Aji, 2019), neglecting the land cover categories. Land cover categories can provide substantial prior knowledge and play an important role in RS image retrieval (Cheng et al., 2017). To shrink the search space and alleviate the difficulties in aligning cross-modal features, we propose scene label augmentation, which aims to provide prior knowledge of scene categories.

More specifically, we regard RS scene categories as metadata tags and combine the metadata with fine-grained content data. Different scenario categories are added in front of content-based descriptions as the prompt (Yuan et al., 2023), as shown in Fig. 1. The augmented captions include scene categories and content information that can be represented as:

$$\mathbf{t} = \text{Concat}(\mathbf{t}_{meta}, \mathbf{t}_{cont}), \quad (14)$$

$$\mathbf{s}^0 = \mathbf{M}_E \cdot \mathbf{t} + \mathbf{T}_{pos}. \quad (15)$$

where \mathbf{t}_{meta} refers the prompt token of metadata, \mathbf{t}_{cont} represents the token of fine-grained content data, \mathbf{M}_E refers the word embedding matrix of BERT, \mathbf{T}_{pos} is the position embedding matrix and \mathbf{s}^0 represents the semantic feature after applying scene label augmentation.

It is worth noting that the designed prompt of the scenario category does not require training. Its vector representation is embedded by the word embedding matrix, which does not require computing gradients and updates. Therefore, our concise and effective augmentation method not only does not incur additional computational overhead but also leverages the prior knowledge contained in scene categories.

3.4. Negative sample recycling

In traditional methods, the sampling pool of negative samples is limited to the size of mini-batch data, which is constrained by the available GPU memory (Pan et al., 2023b). To address this issue, inspired by (He et al., 2020), we innovatively propose the negative sample recycling strategy to expand the pool of negative samples. We establish two distinct negative queues \mathcal{Q}_v and \mathcal{Q}_s to temporarily preserve the negative samples for visual and semantic embeddings, respectively. As shown in Fig. 4, the training data at the previous time step $t - 1$ is recycled as negative samples for the contrastive learning of current data at step t . The queues \mathcal{Q}_v and \mathcal{Q}_s are updated once per iteration, and negative samples from different iterations are maintained first in, first out. The proposed two negative queues \mathcal{Q}_v and \mathcal{Q}_s expand the negative sample pool by decoupling it from the mini-batch size. It is achieved without introducing additional encoders and considerable computational loads.

For one positive pair (s_e, v_e) in text–image retrieval, the negative sample pool is defined as the samples from the negative queue \mathcal{Q}_v that have different scenario categories compared to the positive sample v_e . For training stability, we adopt the difficulty-weighted hinge loss (Zhang et al., 2023) to measure the alignment between the current samples and the negative samples from queues \mathcal{Q}_v and \mathcal{Q}_s :

$$l_v = [\alpha - S(s_e, v_e) + S(s_e, q_v)]_+, \quad (16)$$

$$l_s = [\alpha - S(v_e, s_e) + S(v_e, q_s)]_+, \quad (17)$$

$$L_{queue} = \sum_{q_v \in \mathcal{Q}_v} l_v e^{-\beta l_v} + \sum_{q_s \in \mathcal{Q}_s} l_s e^{-\beta l_s}. \quad (18)$$

where (s_e, v_e) is one positive sample pair, (s_e, q_v) is one negative sample pair, q_v and q_s are negative samples in the queues \mathcal{Q}_v and \mathcal{Q}_s , and margin α controls the margin of the feature alignment. $S(\cdot)$ stands for cosine similarity function. $[x]_+ \equiv \max(x, 0)$.

The L_{batch} loss measures the alignment error when the negative samples are from the current batch data, which can be expressed as:

$$p_{i2i}(I, T) = \frac{\exp(S(I, T)/\tau)}{\exp(S(I, T)/\tau) + \sum_{\hat{I}} \exp(S(\hat{I}, T)/\tau)}, \quad (19)$$

$$p_{i2t}(I, T) = \frac{\exp(S(I, T)/\tau)}{\exp(S(I, T)/\tau) + \sum_{\hat{T}} \exp(S(I, \hat{T})/\tau)}, \quad (20)$$

$$L_{batch} = -\frac{1}{2} E_{(I, T) \sim D} [\log(p_{i2t}(I, T)) + \log(p_{i2i}(I, T))]. \quad (21)$$

where (I, T) refers the positive pair, \hat{I} and \hat{T} refers the negative sample from current batch, and τ servers as the temperature coefficient. $p_{i2i}(I, T)$ represents the matching probability of the positive pair (I, T) when performing text-image retrieval.

The negative sample queues \mathcal{Q}_v and \mathcal{Q}_s are updated by current batch data. The parameters θ_f in the Focus-Adapter and the parameters θ_l in the LoRA module are updated according to the final objective function L :

$$L = L_{batch} + L_{queue}. \quad (22)$$

Table 1
Performance of Different Methods on the RSITMD Test Set

Methods	Backbone (Vision / Text)	Training Params	Image-Query-Text			Text-Query-Image			mR
			R@1	R@5	R@10	R@1	R@5	R@10	
CNN-based methods									
AMFMN	ResNet-18 / GRU	36.70M	10.63	24.78	41.81	11.51	34.69	54.87	29.72
MCRN	ResNet-18 / GRU	52.35M	13.27	29.42	41.59	9.42	35.53	52.74	30.33
HVSA	ResNet-18 / GRU	35.01M	13.20	32.08	45.58	11.43	39.20	57.45	33.16
SWAN	ResNet-50 / GRU	-	13.35	32.15	46.90	11.24	40.40	60.60	34.11
Transformer-based methods									
Single Language	ViT-B-32 / BERT	151M	19.69	40.26	54.42	17.61	49.73	66.59	41.38
IEFT	Vision Trans / BERT	100.12M	11.19	38.09	58.84	15.49	37.61	51.40	35.44
PIR	Swin-T+ResNet50 / BERT	-	18.14	41.15	52.88	12.17	41.68	63.41	38.24
Linear probe	ViT-B-32 / BERT	0.53M	13.71	33.41	48.01	10.97	36.85	56.15	33.18
Cross-Modal Adapter	ViT-B-32 / BERT	0.16M	18.16	36.08	48.72	16.31	44.33	64.75	38.06
PE-RSITR	ViT-B-32 / BERT	0.16M	23.67	44.07	60.36	20.10	50.63	67.97	44.47
CLIP-adapter	ViT-B-32 / BERT	3.04M	20.57	42.03	54.86	17.78	46.68	62.56	40.75
CLIP-lora	ViT-B-32 / BERT	3.93M	21.68	41.37	56.19	16.85	47.25	67.74	41.85
CLIP-bitfit	ViT-B-32 / BERT	0.17M	21.01	42.25	52.21	14.95	45.13	64.29	39.97
CLIP-adapter	ViT-B-16 / BERT	3.04M	21.90	41.81	53.09	17.83	46.94	66.19	41.29
CLIP-lora	ViT-B-16 / BERT	3.93M	22.34	43.14	57.74	19.02	51.46	69.69	43.90
CLIP-bitfit	ViT-B-16 / BERT	0.17M	23.67	42.10	55.45	18.33	48.12	67.35	42.50
CLIP-adapter	ViT-L-14 / BERT	6.82M	25.44	41.15	54.64	18.80	50.08	67.61	42.95
CLIP-lora	ViT-L-14 / BERT	8.65M	26.99	45.35	56.63	21.94	55.26	71.72	46.32
CLIP-bitfit	ViT-L-14 / BERT	0.37M	26.54	41.15	54.64	20.04	51.15	69.29	43.80
CMER(ours)	ViT-B-32 / BERT	2.72M	21.82	47.64	62.24	16.38	53.49	79.70	46.88
CMER(ours)	ViT-B-16 / BERT	2.72M	21.90	48.89	62.46	18.30	55.36	80.82	47.96
CMER(ours)	ViT-L-14 / BERT	4.50M	23.67	49.77	63.93	17.25	56.41	81.15	48.70
CMER(ours)	ViT-H-14 / BERT	9.14M	27.87	54.64	65.92	23.14	58.45	80.75	51.80

4. Experiments and analysis

4.1. Datasets and protocols

Our proposed model is validated on two standard RSTIR datasets, RSICD and RSITMD. The RSICD, proposed by Lu et al. (2017), comprises 10,921 images. Each image in the RSICD is associated with five descriptive texts, yielding $10,921 \times 5$ paired samples. Compared to the RSICD, the RSITMD (Yuan et al., 2021) is smaller and more fine-grained in query. The RSITMD consists of 4,743 images. Each image in the RSITMD is associated with five descriptive texts, yielding $4,743 \times 5$ paired samples. The resolution of images in the RSITMD is standardized to 256×256 pixels.

To reflect the training consumption, the number of training parameters (M), peak GPU memory usage (MB), and the throughput of training data are introduced (pairs/s). The evaluation metrics for model performance are the widely recognized $R@k$ and mR :

$$mR = \frac{1}{|K|} \sum_{k \in K} R@k. \quad (23)$$

where k usually takes the common values of 1, 5, and 10. mR denotes the average value for different values $R@k$ where k belongs to the common value set K .

4.2. Implementation details

All experiments in this paper are implemented on two NVIDIA V100 GPUs, and the weights that achieve the best performance on the validation set are saved. Taking our proposed CMER with the ViT-B-16 backbone as an example, we fix three random seeds to ensure repeatability and reliability. The average of three runs with different random seeds represents the overall performance. We choose AdamW as the optimizer and train with a batch size of 256 for 20 epochs. The initial learning rate is 5×10^{-4} .

Table 2
Performance of Different Methods on the RSICD Test Set

Methods	Backbone (Vision / Text)	Training Params	Image-Query-Text			Text-Query-Image			mR
			R@1	R@5	R@10	R@1	R@5	R@10	
CNN-based methods									
AMFMN	ResNet-18 / GRU	36.70M	5.21	14.72	21.57	4.08	17.00	30.60	15.53
MCRN	ResNet-18 / GRU	52.35M	6.59	19.40	30.28	5.03	19.38	32.99	18.95
HVSA	ResNet-18 / GRU	35.01M	7.47	20.62	32.11	5.51	21.13	34.13	20.16
SWAN	ResNet-50 / GRU	-	7.41	20.13	30.86	5.56	22.26	37.41	20.61
Transformer-based methods									
Single Language	ViT-B-32 / BERT	151M	10.70	29.64	41.53	9.14	28.96	44.59	27.42
IEFT	Vision Trans / BERT	100.12M	8.38	28.17	44.16	8.78	28.47	43.88	26.97
PIR	Swin-T+ResNet50 / BERT	-	9.88	27.26	39.16	6.97	24.56	38.92	24.46
Linear probe	ViT-B-32 / BERT	0.53M	8.46	24.41	37.72	7.81	25.89	42.47	24.46
Cross-Modal Adapter	ViT-B-32 / BERT	0.16M	11.18	27.31	40.62	9.57	30.74	48.36	27.96
PE-RSITR	ViT-B-32 / BERT	0.16M	14.13	31.51	44.78	11.63	33.92	50.73	31.12
CLIP-adapter	ViT-B-32 / BERT	3.04M	13.99	31.01	44.46	10.21	31.54	46.62	29.64
CLIP-lora	ViT-B-32 / BERT	3.93M	14.82	32.66	44.92	12.04	33.87	49.75	31.34
CLIP-bitfit	ViT-B-32 / BERT	0.17M	13.72	32.47	44.83	11.45	32.46	49.02	30.66
CLIP-adapter	ViT-B-16 / BERT	3.04M	14.36	31.65	44.46	11.60	32.68	48.32	30.51
CLIP-lora	ViT-B-16 / BERT	3.93M	16.01	33.66	44.83	11.65	33.52	49.64	31.55
CLIP-bitfit	ViT-B-16 / BERT	0.17M	15.55	33.02	47.30	11.60	33.79	49.97	31.87
CLIP-adapter	ViT-L-14 / BERT	6.82M	15.00	34.03	47.39	11.83	34.78	51.01	32.34
CLIP-lora	ViT-L-14 / BERT	8.65M	15.73	35.95	48.58	13.10	38.40	53.37	34.19
CLIP-bitfit	ViT-L-14 / BERT	0.37M	16.10	36.13	48.85	12.64	36.26	53.04	33.84
CMER(ours)	ViT-B-32 / BERT	2.72M	13.29	31.01	43.15	9.76	32.58	50.81	30.10
CMER(ours)	ViT-B-16 / BERT	2.72M	14.15	32.29	46.56	10.61	32.10	50.33	31.01
CMER(ours)	ViT-L-14 / BERT	4.50M	15.55	35.49	49.03	10.66	33.41	51.49	32.61
CMER(ours)	ViT-H-14 / BERT	9.14M	17.56	35.22	48.67	12.66	37.54	55.24	34.48

Table 3
Efficiency Of Different Methods

	CLIP-adapter	CLIP-bitfit	CLIP-lora	CLIP-adapter	CLIP-bitfit	CLIP-lora	CMER(ours)	CMER(ours)	CMER(ours)
Vision Backbone	ViT-B-16	ViT-B-16	ViT-B-16	ViT-L-14	ViT-L-14	ViT-L-14	ViT-B-16	ViT-L-14	ViT-H-14
Training Params(M)	3.04	0.17	3.93	6.82	0.37	8.65	2.72	4.50	9.14
Memory(MB)	6841	6921	7173	22015	21740	22435	3488	12450	18235
Throughput(pairs/s)	200	191	137	48	47	35	276	83	35

4.3. Performance comparisons

The proposed CMER is compared with recent well-performed RSTIR methods in this subsection. The results are shown in Tables 1 and 2.

Results on RSITMD: In Table 1, we show the results of CMER as well as comparisons with the recent superior methods on the RSITMD test set. The best results are highlighted in bold. From the results, our proposed CMER surpasses the recent state-of-the-art method with a clear margin. When compared with CNN-based methods, our CMER method outperforms SWAN by 12.77% in overall retrieval performance (mR). When compared with Transformer-based methods on ViT-B-32, our CMER method outperforms the Single Language method by 13.11% in text-to-image retrieval (R@10) and 5.50% in overall retrieval performance. The proposed CMER (ViT-B-32) also surpasses the previous state-of-the-art method PE-RSITR by 11.73% in text-to-image retrieval (R@10) and 2.41% in overall retrieval performance. Our CMER achieves the best mR of 51.80% on ViT-H-14.

Results on RSICD: We report results for the RSICD test set in Table 2, where the proposed CMER outperforms many recent advanced methods. Our method is remarkably ahead of traditional CNN-based methods. When compared with Transformer-based methods, our CMER (ViT-B-32) outperforms the IEFT by 3.13% in metric mR. Compared to CLIP-adapter, our CMER (ViT-B-32) achieves a relative improvement of 8.98% in image retrieval (R@10). Our

Table 4
Ablation Experiments of CMER on the RSICD and RSITMD

Ablation Model	Semantic Encoder LoRA	Visual Encoder Focus-Adapter	Training Data		Consumption		mR	
			Negative Recycling	Scene Prompt	Memory	Throughput	RSICD	RSITMD
v1	✓				13153 MB	338 pairs/s	25.94	34.07
v2	✓	✓			19327 MB	276 pairs/s	29.49	40.59
d1	✓	✓	✓		19331 MB	274 pairs/s	29.76	40.81
d2	✓	✓	✓	✓	19331 MB	274 pairs/s	31.01	47.96

CMER (ViT-H-14) achieves a 3.50% relative improvement in text-to-image retrieval (R@10) compared to the recent excellent model CLIP-lora (ViT-L-14).

Comparison of Efficiency: Table 3 shows the efficiency of different methods during the training process. Compared with the excellent method CLIP-lora on ViT-B-16, our proposed CMER method reduces memory usage by 51% and has a 2.0 times data throughput. Our proposed CMER also has a 1.4 times data throughput and reduces memory usage by 49% compared to the baseline method CLIP-adapter on the ViT-B-16. The training resource consumption of CMER on ViT-H is on the same level as that of traditional methods on ViT-L. Our CMER is not only more efficient in resources but also has a competitive overall performance. Combined with the results in Tables 1 and 2, our approach achieves competitive results under the same constraints of resource consumption, realizing a better trade-off between resource consumption and performance.

4.4. Ablation studies

4.4.1. Analyze Each Component in the CMER

To systematically explore the effect of different components in the CMER, we have performed ablation experiments on both the RSICD and RSITMD, as shown in Table 4.

The semantic encoder remains consistent across all experiments, consisting of the LoRA modules and the BERT model (Hu et al., 2021). Comparing the v1 model with the v2, the introduction of the Focus-Adapter in v2 improves the mR metric by 3.55% on the RSICD and 6.52% on the RSITMD. The proposed Focus-Adapter effectively provides the complementary region information to the backbone and suppresses background interference.

The comparison between the v2 and the d1 models demonstrates the validity of the negative sample recycling strategy. During training, the peak GPU memory usage increases by only 4MB, and the data throughput decreases by 2 pairs/s. The proposed negative sample recycling strategy decouples the sampling pool of negative samples from the batch size, which contributes to sampling the high-dimensional semantic space.

Compared to the d2 model with the d1, the scene label augmentation has brought improvements of 1.25% and 7.15% in the mR metric for the RSICD and RSITMD, respectively. Notably, the d2 and d1 models have the same memory footprint and data throughput. Our plug-and-play augmentation technique effectively shrinks the search space, significantly improves the retrieval accuracy, and does not involve additional computational overhead.

4.4.2. Hyperparameters of the Focus-Adapter

Different hidden layer dimensions and sizes of the focus field in the focus layer have varying impacts on the CMER performance, as shown in Table 5. The pre-trained ViT-B-16 model is utilized on the RSITMD to perform a preliminary grid search for hyperparameters of the Focus-Adapter. The TQI in Table 5 represents the performance of Text-Query-Image. We sum all R@k in text-query-image to obtain the TQI, and the IQT is calculated similarly. The hidden dimension takes common values of 128, 192, and 256, corresponding to the number of heads in multi-head attention as 4, 6, and 8, respectively. The head's dimension is fixed at 32. The size of focus fields are set to 1, 2, and 7. When the dimension of the hidden layer is 192, and the size of the focus field is 2, the best performance is obtained.

4.4.3. Hyperparameters of the negative queues

We explore the impact of queue length in the proposed negative sample recycling strategy, and the results on the RSITMD are listed in Table 6. The appropriate length for the negative sample queue should be 4 times the batch size, which is the sum of the negative samples over 4 iterations. When the negative sample pool is expanded to four times the batch size, the text-to-image retrieval performance increases by 1.87 points, and the overall performance increases by 0.22%. However, when too many negative samples are recycled, it leads to performance degradation instead. We

Table 5

Experiments of the Focus Layer.

Hidden Dim	Focus Field	Head	IQT	TQI	mR
128	1	4	113.69	127.46	40.19
128	2	4	113.34	128.36	40.28
128	7	4	112.51	127.21	39.95
192	1	6	114.75	127.38	40.35
192	2	6	114.06	129.49	40.59
192	7	6	112.08	127.46	39.92
256	1	8	113.48	127.79	40.21
256	2	8	110.82	129.32	40.02
256	7	8	114.89	126.45	40.22

Table 6

Grid Search for the Length of Queues on the RSITMD

Length	0	2	4	8
IQT	114.06	113.43	113.51	113.91
TQI	129.49	130.66	131.36	130.48
mR	40.59	40.68	40.81	40.73

suggest that excessively stale data hinders the learning of discriminative features from the currently useful data as parameters are updated.

4.5. Qualitative analysis

4.5.1. Focus-Adapter

To reflect the contribution of the Focus-Adapter intuitively, we visualize the visual features extracted by the visual encoder. For each text query, heatmaps of the different methods on the positive pairs are visualized by the Grad-Cam (Selvaraju et al., 2017).

In Fig. 5(a), compared to the v1 method in subsection 4.4, our approach effectively filters the interference of river pixels, focusing more on the bridge. Similarly to Fig. 5(a), in Fig. 5(b), the baseline method does not focus well on the swimming pool, mainly due to interference from trees and grass, while our proposed method performs better. As shown in Fig. 5(c) and Fig. 5(d), the primary entities are the football field and pond, which have a relatively large pixel proportion. Our method also performs well in RS images with relatively large regions of interest. The above visualization experiments further demonstrate the effectiveness of the focus layer in suppressing background interference when extracting features of small entities.

4.5.2. Modal entanglement visualization

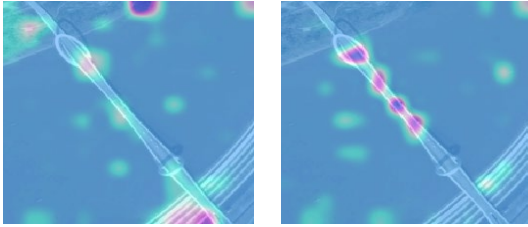
The t-SNE algorithm (Van der Maaten and Hinton, 2008) is employed to visualize high-dimensional cross-modal features. Figure 6(a) illustrates that the boundaries between different clusters are somewhat ambiguous in the baseline method CLIP-lora. As shown in Fig. 6(b), the proposed CMER method demonstrates an enhanced ability to differentiate semantic features across various scenes.

4.5.3. Bad case studies

To investigate the limitations of the CMER method, we specifically identify some typical failed retrieval results on the RSICD. We suggest that the performance of our method is mainly limited by modeling capacity and data quality.

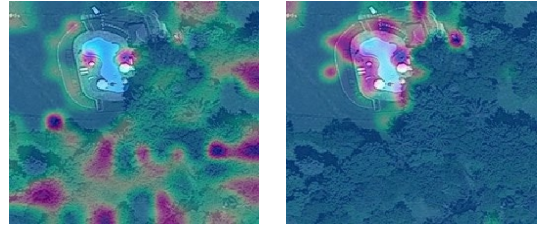
As shown in Fig. 7, inaccurate quantity information extraction is a noticeable weakness of CMER. When the query text explicitly states that there are three ponds. Based solely on the quantity information of ponds, the correct match should ideally rank first or second, rather than fourth. Figure 7 (b) is similar to Figure 7 (a), where the image at rank 1 does indeed have two rivers, but there are no bridges. We believe that subsequent improvements can be achieved by boosting the object-counting ability for the proposed CMER.

Query: There is a **twin-tower bridge** across the river.



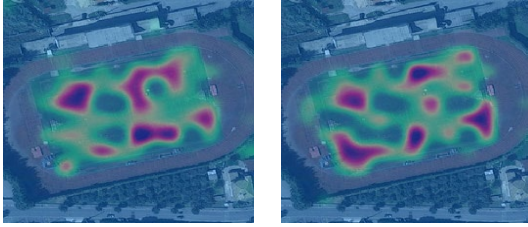
(a)

Query: There is a **swimming pool** on the grass, half covered with trees.



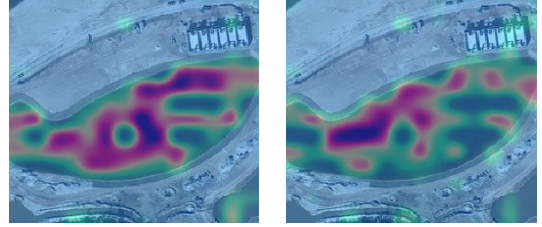
(b)

Query: On the side of the road is a **playground**, a forest belt and some buildings.



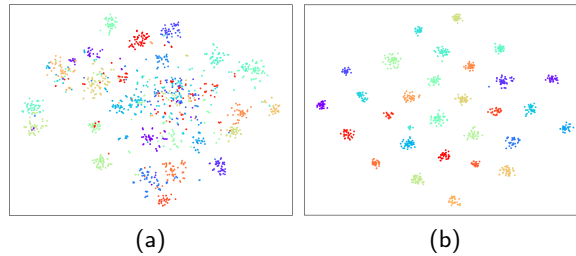
(c)

Query: Several **buildings** and **bare land** are around an oval **pond**.



(d)

Figure 5: Qualitative results of the proposed Focus-Adapter. In (a) and (b), the primary entities described in the text are relatively small in scale, with a large proportion of background pixels. In (c) and (d), the primary entities described in the text are relatively large in scale.



(a)

(b)

Figure 6: The visualization of high-dimensional cross-modal features. In (a) and (b), dots with different colors represent semantic features from different scene categories.

Dataset quality issues such as semantic concept ambiguity and high query text similarity are common challenges for RSTIR (Zhang et al., 2023), (Yuan et al., 2021). As shown in Fig. 8, we present examples where ground truth images are not among the top 5 retrieval results. According to the query text in Fig. 8(a), almost all retrieved results can be described as “spacious airports”, but the annotated ground truth does not rank in the top 5. In Fig. 8(b), the first, second, and fourth RS images contain storage tanks and factory elements, satisfying the “build-in” relationship. Therefore, efforts to further improve the quality and quantity of the dataset are worthwhile, including more fine-grained, rich content description texts.

5. Conclusion

In this work, we propose the novel CMER for RSTIR to enhance the resource efficiency of transfer learning. The Focus-Adapter adopts the side branch structure. Its focus layer can reduce the background interference when extracting features of small targets. Moreover, the scene label prompt augmentation and the negative sample recycling strategy enhance the efficacy of data and improve the generalization performance of retrieval. Our CMER has a superior overall

Query: Three ponds with different shapes are beautiful.



(a)

Query: Two green rivers join together with a bridge spans it.



(b)

Figure 7: Failed text-image retrieval cases due to insufficient CMER capacity. The retrieved images are organized from left to right according to their similarity to the query text. The top 5 retrieved images are shown, with red boxes indicating negative matches and green boxes indicating positive matches.

Query: The airport is very spacious.



(a)

Query: Many storage tanks are built in the factory.



(b)

Figure 8: Failed text-image retrieval cases due to the semantic ambiguity in the RSICD.

performance under equivalent resource constraints, which has been validated by sufficient experiments on various classical datasets.

In our future work, we would like to boost the object counting ability of our framework, addressing the issue of mismatched quantity information. We also hope to improve the quality and quantity of the dataset, achieving fine-grained alignment of significant instances with rich content description texts.

References

- Al Rahhal, M.M., Bazi, Y., Alsharif, N.A., Bashmal, L., Alajlan, N., Melgani, F., 2022. Multilanguage transformer for improved text to remote sensing image retrieval. *IEEE Journal of Selected Topics in Applied Earth Observations and Remote Sensing* 15, 9115–9126.
- Amani, M., Ghorbanian, A., Ahmadi, S.A., Kakooei, M., Moghimi, A., Mirmazloumi, S.M., Moghaddam, S.H.A., Mahdavi, S., Ghahremanloo, M., Parsian, S., et al., 2020. Google earth engine cloud computing platform for remote sensing big data applications: A comprehensive review. *IEEE*

- Journal of Selected Topics in Applied Earth Observations and Remote Sensing 13, 5326–5350.
- Blumenstiel, B., Moor, V., Kienzler, R., Brunschwiler, T., 2024. Multi-spectral remote sensing image retrieval using geospatial foundation models. arXiv preprint arXiv:2403.02059 .
- Chen, Y., Huang, J., Li, X., Xiong, S., Lu, X., 2023. Multiscale salient alignment learning for remote sensing image-text retrieval. IEEE Transactions on Geoscience and Remote Sensing .
- Cheng, G., Han, J., Lu, X., 2017. Remote sensing image scene classification: Benchmark and state of the art. Proceedings of the IEEE 105, 1865–1883.
- Chi, M., Plaza, A., Benediktsson, J.A., Sun, Z., Shen, J., Zhu, Y., 2016. Big data for remote sensing: Challenges and opportunities. Proceedings of the IEEE 104, 2207–2219.
- Devlin, J., Chang, M.W., Lee, K., Toutanova, K., 2018. Bert: Pre-training of deep bidirectional transformers for language understanding. arXiv preprint arXiv:1810.04805 .
- Djoufack Basso, L., 2022. CLIP-RS: A Cross-modal Remote Sensing Image Retrieval Based on CLIP, a Northern Virginia Case Study. Ph.D. thesis. Virginia Tech.
- Dosovitskiy, A., Beyer, L., Kolesnikov, A., Weissenborn, D., Zhai, X., Unterthiner, T., Dehghani, M., Minderer, M., Heigold, G., Gelly, S., et al., 2020. An image is worth 16x16 words: Transformers for image recognition at scale. arXiv preprint arXiv:2010.11929 .
- Edalati, A., Tahaei, M., Kobzyev, I., Nia, V.P., Clark, J.J., Rezagholizadeh, M., 2022. Krona: Parameter efficient tuning with kronecker adapter. arXiv preprint arXiv:2212.10650 .
- Espinoza-Molina, D., Datcu, M., 2013. Earth-observation image retrieval based on content, semantics, and metadata. IEEE Transactions on Geoscience and Remote Sensing 51, 5145–5159.
- Fang, Y., Li, P., Zhang, J., Ren, P., 2021. Cohesion intensive hash code book coconstruction for efficiently localizing sketch depicted scenes. IEEE Transactions on Geoscience and Remote Sensing 60, 1–16.
- He, K., Fan, H., Wu, Y., Xie, S., Girshick, R., 2020. Momentum contrast for unsupervised visual representation learning, in: Proceedings of the IEEE/CVF conference on computer vision and pattern recognition, pp. 9729–9738.
- He, K., Zhang, X., Ren, S., Sun, J., 2016. Deep residual learning for image recognition, in: Proceedings of the IEEE conference on computer vision and pattern recognition, pp. 770–778.
- Houlsby, N., Giurgiu, A., Jastrzebski, S., Morrone, B., De Laroussilhe, Q., Gesmundo, A., Attariyan, M., Gelly, S., 2019. Parameter-efficient transfer learning for nlp, in: International conference on machine learning, PMLR. pp. 2790–2799.
- Hu, E.J., Shen, Y., Wallis, P., Allen-Zhu, Z., Li, Y., Wang, S., Wang, L., Chen, W., 2021. Lora: Low-rank adaptation of large language models. arXiv preprint arXiv:2106.09685 .
- Jiang, H., Zhang, J., Huang, R., Ge, C., Ni, Z., Lu, J., Zhou, J., Song, S., Huang, G., 2022. Cross-modal adapter for text-video retrieval. arXiv preprint arXiv:2211.09623 .
- Lei, T., Bai, J., Brahma, S., Ainslie, J., Lee, K., Zhou, Y., Du, N., Zhao, V., Wu, Y., Li, B., et al., 2024. Conditional adapters: Parameter-efficient transfer learning with fast inference. Advances in Neural Information Processing Systems 36.
- Li, G., Qian, M., Xia, G.S., 2024a. Unleashing unlabeled data: A paradigm for cross-view geo-localization. arXiv preprint arXiv:2403.14198 .
- Li, J., Li, D., Savarese, S., Hoi, S., 2023. Blip-2: Bootstrapping language-image pre-training with frozen image encoders and large language models, in: International conference on machine learning, PMLR. pp. 19730–19742.
- Li, J., Selvaraju, R., Gotmare, A., Joty, S., Xiong, C., Hoi, S.C.H., 2021. Align before fuse: Vision and language representation learning with momentum distillation. Advances in neural information processing systems 34, 9694–9705.
- Li, P., Han, L., Tao, X., Zhang, X., Grecos, C., Plaza, A., Ren, P., 2020. Hashing nets for hashing: A quantized deep learning to hash framework for remote sensing image retrieval. IEEE Transactions on Geoscience and Remote Sensing 58, 7331–7345.
- Li, X., Wen, C., Hu, Y., Yuan, Z., Zhu, X.X., 2024b. Vision-language models in remote sensing: Current progress and future trends. IEEE Geoscience and Remote Sensing Magazine .
- Lialin, V., Deshpande, V., Rumshisky, A., 2023. Scaling down to scale up: A guide to parameter-efficient fine-tuning. arXiv preprint arXiv:2303.15647 .
- Liu, A.A., Yang, B., Li, W., Song, D., Sun, Z., Ren, T., Wei, Z., 2024a. Text-guided knowledge transfer for remote sensing image-text retrieval. IEEE Geoscience and Remote Sensing Letters .
- Liu, F., Chen, D., Guan, Z., Zhou, X., Zhu, J., Ye, Q., Fu, L., Zhou, J., 2024b. Remoteclip: A vision language foundation model for remote sensing. IEEE Transactions on Geoscience and Remote Sensing .
- Lu, X., Wang, B., Zheng, X., Li, X., 2017. Exploring models and data for remote sensing image caption generation. IEEE Transactions on Geoscience and Remote Sensing 56, 2183–2195.
- Ma, Q., Pan, J., Bai, C., 2024. Direction-oriented visual-semantic embedding model for remote sensing image-text retrieval. IEEE Transactions on Geoscience and Remote Sensing .
- Van der Maaten, L., Hinton, G., 2008. Visualizing data using t-sne. Journal of machine learning research 9.
- Mao, G., Yuan, Y., Xiaoqiang, L., 2018. Deep cross-modal retrieval for remote sensing image and audio, in: 2018 10th IAPR workshop on pattern recognition in remote sensing (PRRS), IEEE. pp. 1–7.
- Ning, H., Zhao, B., Yuan, Y., 2021. Semantics-consistent representation learning for remote sensing image-voice retrieval. IEEE Transactions on Geoscience and Remote Sensing 60, 1–14.
- Pan, J., Ma, Q., Bai, C., 2023a. A prior instruction representation framework for remote sensing image-text retrieval, in: Proceedings of the 31st ACM International Conference on Multimedia, pp. 611–620.
- Pan, J., Ma, Q., Bai, C., 2023b. Reducing semantic confusion: Scene-aware aggregation network for remote sensing cross-modal retrieval, in: Proceedings of the 2023 ACM International Conference on Multimedia Retrieval, pp. 398–406.
- Pratt, L.Y., 1992. Discriminability-based transfer between neural networks. Advances in neural information processing systems 5.

- Radford, A., Kim, J.W., Hallacy, C., Ramesh, A., Goh, G., Agarwal, S., Sastry, G., Askell, A., Mishkin, P., Clark, J., et al., 2021. Learning transferable visual models from natural language supervision, in: International conference on machine learning, PMLR. pp. 8748–8763.
- Ren, P., Tao, Y., Han, J., Li, P., 2023. Hashing for geo-localization. *IEEE Transactions on Geoscience and Remote Sensing* .
- Selvaraju, R.R., Cogswell, M., Das, A., Vedantam, R., Parikh, D., Batra, D., 2017. Grad-cam: Visual explanations from deep networks via gradient-based localization, in: Proceedings of the IEEE international conference on computer vision, pp. 618–626.
- Sudha, S., Aji, S., 2019. A review on recent advances in remote sensing image retrieval techniques. *Journal of the Indian Society of Remote Sensing* 47, 2129–2139.
- Sun, Y., Ye, Y., Kang, J., Fernandez-Beltran, R., Ban, Y., Hafner, S., Li, X., Luo, C., Plaza, A., 2024. Cross-modal hashing with feature semi-interaction and semantic ranking for remote sensing ship image retrieval. *IEEE Transactions on Geoscience and Remote Sensing* .
- Sun, Y., Ye, Y., Kang, J., Fernandez-Beltran, R., Ban, Y., Li, X., Zhang, B., Plaza, A., 2022. Multisource data reconstruction-based deep unsupervised hashing for unisource remote sensing image retrieval. *IEEE Transactions on Geoscience and Remote Sensing* 60, 1–16. doi:10.1109/TGRS.2022.3231215.
- Sun, Y., Ye, Y., Kang, J., Fernandez-Beltran, R., Li, X., Xiong, Z., Huang, X., Plaza, A., 2023. Consistency center-based deep cross-modal hashing for multisource remote sensing image retrieval. *IEEE Transactions on Geoscience and Remote Sensing* 61, 1–16. doi:10.1109/TGRS.2023.3323495.
- Tang, X., Wang, Y., Ma, J., Zhang, X., Liu, F., Jiao, L., 2023. Interacting-enhancing feature transformer for cross-modal remote sensing image and text retrieval. *IEEE Transactions on Geoscience and Remote Sensing* .
- Vaswani, A., Shazeer, N., Parmar, N., Uszkoreit, J., Jones, L., Gomez, A.N., Kaiser, Ł., Polosukhin, I., 2017. Attention is all you need. *Advances in neural information processing systems* 30.
- Xiong, W., Xiong, Z., Cui, Y., Huang, L., Yang, R., 2022. An interpretable fusion siamese network for multi-modality remote sensing ship image retrieval. *IEEE Transactions on Circuits and Systems for Video Technology* .
- Yuan, Y., Zhan, Y., Xiong, Z., 2023. Parameter-efficient transfer learning for remote sensing image-text retrieval. *IEEE Transactions on Geoscience and Remote Sensing* .
- Yuan, Z., Zhang, W., Fu, K., Li, X., Deng, C., Wang, H., Sun, X., 2021. Exploring a fine-grained multiscale method for cross-modal remote sensing image retrieval. *IEEE Transactions on Geoscience and Remote Sensing* 60, 1–19.
- Yuan, Z., Zhang, W., Tian, C., Mao, Y., Zhou, R., Wang, H., Fu, K., Sun, X., 2022. Mcrn: A multi-source cross-modal retrieval network for remote sensing. *International Journal of Applied Earth Observation and Geoinformation* 115, 103071.
- Zaken, E.B., Ravfogel, S., Goldberg, Y., 2021. Bitfit: Simple parameter-efficient fine-tuning for transformer-based masked language-models. *arXiv preprint arXiv:2106.10199* .
- Zhang, J.O., Sax, A., Zamir, A., Guibas, L., Malik, J., 2020. Side-tuning: a baseline for network adaptation via additive side networks, in: *Computer Vision—ECCV 2020: 16th European Conference, Glasgow, UK, August 23–28, 2020, Proceedings, Part III 16*, Springer. pp. 698–714.
- Zhang, W., Li, J., Li, S., Chen, J., Zhang, W., Gao, X., Sun, X., 2023. Hypersphere-based remote sensing cross-modal text-image retrieval via curriculum learning. *IEEE Transactions on Geoscience and Remote Sensing* .
- Zhou, W., Guan, H., Li, Z., Shao, Z., Delavar, M.R., 2023. Remote sensing image retrieval in the past decade: Achievements, challenges, and future directions. *IEEE Journal of Selected Topics in Applied Earth Observations and Remote Sensing* .